# Magnetic dipole moments, electric quadrupole moments, and electron scattering form factors of neutron-rich *sd-pf* cross-shell nuclei

R. A. Radhi,[1] Ali A. Alzubadi,[1] and A. H. Ali[2]
[1]*Department of Physics, College of Science, University of Baghdad, Baghdad, Iraq*
[2]*College of Medicine, University of Fallujah, Fallujah, Iraq*

(Received 20 March 2018; published 15 June 2018)

Magnetic dipole and electric quadrupole moments are calculated for neutron-rich *sd-pf* cross-shell nuclei. These nuclei include open shell isotopes with the number of protons less than 20 and neutrons greater than 20, for which experimental data are available. Shell model calculations are performed with full *sd* shell model space for $Z-8$ valence protons and full *pf* shell model space for $N-20$ valence neutrons, where the remaining 20 neutrons are frozen in *s*, *p* and *sd*-shells. Also, magnetic and Coulomb electron scattering form factors are calculated for some of these nuclei. Excitation out of major shell space are taken into account through a microscopic theory which allows particle-hole excitation from the core and model space orbits to all higher orbits with $2\hbar\omega$ excitation. Effective charges are obtained for each isotope. Core polarization (CP) is essential for obtaining a reasonable description of the electric quadrupole moments and enhance the Coulomb form factors but has no effect on the dipole magnetic moments but squeezes the magnetic form factors. The magnetic static and dynamic properties can be described by free *g* factors for the model space nucleons without introducing CP effect, on the contrary to the electric static and dynamic properties, which cannot be described properly by the model space nucleons without taking into account CP effects.

DOI: 10.1103/PhysRevC.97.064312

## I. INTRODUCTION

The study of neutron-rich nuclei far from the stability line is considered as a valuable tool for understanding nuclear structure. They exhibit properties different from those of stable nuclei. Such properties are called exotic and deserve theoretical and experimental investigations. Nuclear deformation is considered as one of the most striking features in neutron-rich nuclei, and can be investigated theoretically and experimentally through their electromagnetic properties, electric quadrupole ($Q$) moments, magnetic dipole ($\mu$) moments, and so on. Sagawa and Asahi [1] have studied the $N/Z$ dependence of the quadrupole polarization charges of C isotopes by using a microscopic particle-vibration model in which Hartree-Fock and random-phase approximations are used to calculate the single-particle wave functions and giant quadrupole resonances. A large quenching of the polarization charges was found in nuclei with a large $N/Z$ ratio. Ogawa *et al.* [2] showed that the tendency of the $Q$ moment for $^{17}$B stays nearly constant over neutron-rich isotopes, which conflicts with standard shell model calculations, which predict gradual and considerable increase of the $Q$ moment with increasing $N/Z$ ratio. Shell model calculations, however, assume constant values of effective charges, which may not be adequate for the case of extremely neutron-rich nuclei. The Bohr-Mottelson (BM) particle-vibration coupling model for effective charges [3], which involves both the global dependence on $(N-Z)/A$ and the quenching effects for loosely bound particles, has been adopted by Ogawa *et al.* [2] which showed that the experimental $Q$ moments were well reproduced. A least-squares fit with two free parameters gave proton and neutron effective charges, $e_\pi = 1.3e$ and $e_\nu = 0.5e$ [4] for nuclei in the *sd*-shell region. Similar values have been used also in other mass regions, in stable nuclei and those near the beta stability line. A large ratio of proton and neutron quadrupole matrix elements in Be and C isotopes with $N > 8$ suggests the neutron quadrupole motion is decoupled from the proton quadrupole motion and leads to the small neutron effective charge [5]. Theoretical results [6] showed that effective charges are smaller than the standard values in light neutron-rich nuclei and imply decoupled quadrupole motions between protons and neutrons in those nuclei. The description of the ground state properties of some spherical nuclei far from the stability line has been studied by Co *et al.* [7] through the predictions of three mean-field theoretical approaches. The first excited state *g* factors of neutron-rich nuclei near $N = 28$ has been measured [8] by applying the transient-field technique, to investigate the shape change in $^{38}$S and $^{40}$S produced as fast radioactive beams. The contribution of protons to the magnetic moments in these nuclei is balanced by the contribution of the neutrons. The magnetic form factors of the odd-*A* *sd* shell nuclei $^{17}$O, $^{25}$Mg, $^{27}$Al, $^{29}$Si, and $^{31}$P are studied [9] within the relativistic frame with single-nucleon wave functions generated using the relativistic mean-field model. It was found that the single valence-nucleon contributions can generally give a good approximate description for the shapes of the nuclear magnetic form factors, including the positions of the minima and maxima, and after the quenching ratios are applied, the experimental data can be very well reproduced. For neutron-rich nuclei, interactions are derived from chiral effective field theory including three-nucleon forces. These interactions were used to calculate the ground-state magnetic moments of $^{49,51}$Ca and quadrupole

 

moments of $^{47,49,51}$Ca where the measurements have been done for the first time [10]. A model was presented [11] which describes the properties of odd-even nuclei with one nucleon more, or less, with respect to the magic number. This model was applied to the evaluation of electric quadrupole and magnetic dipole moments of odd-even nuclei around oxygen, calcium, zirconium, tin, and lead isotopes. Shell model calculations for electric quadrupole moments and magnetic dipole moments of *sd* shell nuclei have been performed by Saxena and Srivastava [12] using valence-space Hamiltonians derived with two *ab initio* approaches. Their results were in reasonable agreement with the available experimental data as well as with the results from the phenomenological USDB effective interaction [13]. New effective charges for protons and neutrons have been determined by Bouhelal *et al.* [14] as $1.36e$ for protons and $0.48e$ for neutrons for the electric-octupole $E3$ transition strengths from the first $3^-$ state to the ground-state transition in *sd* shell even-even nuclei with $A = 16$–$40$. Their values were close to those obtained previously for electric-quadrupole $E2$ transitions in *sd* shell nuclei.

Electron scattering from exotic unstable nuclei has received wide attention from researchers especially in the theoretical studies due to the importance of this process as a probe for the study of nuclear structure. Garrido *et al.* [15] investigated electron scattering reactions on two-neutron halo nuclei. They considered the case of electron-$^6$He scattering. They also investigated electron scattering reactions on two-neutron halo nuclei in the quasielastic region [16]. Calculations of the charge form factors of exotic light neutron-rich nuclei ($^{6,8}$He, $^{11}$Li, $^{17,19}$B, and $^{14}$Be) have been performed by Antonov *et al.* [17] using various nuclear models. A microscopic large-scale shell model has been performed to calculate charge form factors for light He and Li neutron-rich isotopes, and the deformed self-consistent mean-field Skyrme HF + BCS method for heavier ones Ni, Kr, and Sn [18]. Bertulani [19] has studied the electron scattering of light unstable nuclei giving particular attention to the effect of the neutron (proton) skin on the scattering form factors. It was shown that the noticeable changes in the charge size radius can be interpreted in terms of the position of the first minimum. The conceptual design of the electron-ion scattering experiment (ELISe) has been presented which offers a unique opportunity to use electrons as a probe in investigations of the structure of exotic nuclei [20].

In the present work, we will adopt a shell model with harmonic oscillator (HO) single particle wave functions to calculate the magnetic and quadrupole moments and longitudinal and transverse magnetic form factors for *sd-pf* cross-shell nuclei. Conventional shell model calculations in the full *sdpf* space are not possible because of the huge dimension in the configuration space. Truncation in the valence space is needed. Full *sd* valence space for $Z-8$ protons and full *fp* valence space for $N-20$ neutrons, with freezing 20 neutrons in the *sd* shell are considered with the core-polarization effect through particle-hole excitation.

## II. THEORY

The nuclear matrix element of the electromagnetic ($\hat{O}$) and electron scattering ($\hat{T}$) operators between the initial ($i$) and final ($f$) nuclear states for a given multipolarity $\lambda$ is expressed as the sum of the products of the one-body density matrix (OBDM) times the single-particle matrix elements

$$\langle f||\hat{X}(\lambda)||i\rangle = \sum_{k_a k_b} \mathrm{OBDM}(fik_ak_b\lambda)\langle k_a||\hat{X}(\lambda)||k_b\rangle, \quad (1)$$

where the $\hat{X}$ operator stands for the electromagnetic operator ($\hat{O}$) and the electron scattering operator ($\hat{T}$). The single-particle states ($n\,l\,j$) are denoted by $k$.

The reduced single-particle (SP) matrix elements of the $\hat{X}$ operator are expressed as a sum of the model space (MS) contribution and the core-polarization (CP) contribution, as follows [21]:

$$\begin{aligned}&\langle k_a||\hat{X}(\lambda)||k_b\rangle \\ &= \langle k_a||\hat{X}(\lambda)||k_b\rangle_{\mathrm{MS}} + \left[\left\langle k_a||\hat{X}_\lambda \frac{\hat{Q}}{E_i - H_0}\mathrm{V}_{\mathrm{res}}||k_b\right\rangle\right. \\ &\left. + \left\langle k_a||\mathrm{V}_{\mathrm{res}}\frac{\hat{Q}}{E_f - H_0}\hat{X}_\lambda||k_b\right\rangle\right]_{\mathrm{CP}} \end{aligned} \quad (2)$$

where the operator $\hat{Q}$ is the projection operator onto the space outside the MS. For the residual two-body interaction $V_{\mathrm{res}}$, the two-body Michigan three range Yukawa (M3Y) interaction of Bertsch *et al.* [22] is adopted.

The magnetic dipole moment is defined in terms of the $M1$ operator as [21]

$$\mu = \sqrt{\frac{4\pi}{3}}\begin{pmatrix} J & 1 & J \\ -J & 0 & J\end{pmatrix}\langle J\|\hat{O}(M1)\|J\rangle\mu_N, \quad (3)$$

where $\mu_N$ is the nuclear magneton $\mu_N = \frac{e\hbar}{2m_pc} = 0.1051\ e\mathrm{fm}$.

The electric quadrupole moment is defined as [21]

$$Q = \sqrt{\frac{16\pi}{5}}\begin{pmatrix} J & 2 & J \\ -J & 0 & J\end{pmatrix}\langle J\|\hat{O}(E2)\|J\rangle, \quad (4)$$

where the initial and final nuclear states $|J\rangle$ include all the quantum numbers needed to distinguish the states.

The electron scattering form factor involving angular momentum $\lambda$ and momentum transfer $q$, between the initial ($i$) and final ($f$) nuclear shell model states, is given by [23]

$$|F(\eta\lambda,q)|^2 = \frac{4\pi}{Z^2(2J_i+1)}|\langle f\|\hat{T}(\eta\lambda,q)\|i\rangle F_{\mathrm{c.m}}(q)F_{\mathrm{f.s}}(q)|^2 \quad (5)$$

with $\eta$ selecting the longitudinal or Coulomb (C), and transverse magnetic (M) form factors, respectively.

The finite size (f.s.) nucleon form factor is $F_{\mathrm{f.s}} = [1 + (q/4.33)^2]^{-2}$, and $F_{\mathrm{cm}} = e^{q^2b^2/4A}$ is the correction for the lack of translational invariance in the shell model. $A$ is the mass number, and $b$ is the harmonic oscillator (HO) length parameter. The total transverse magnetic form factors are given by

$$|F(\mathrm{M},q)|^2 = \sum_{\lambda\geqslant 1}|F(M\lambda,q)|^2. \quad (6)$$

The mean square charge radius is defined as [24]

$$\langle r_c^2\rangle = \langle r^2\rangle_p + \langle R_p^2\rangle + \frac{N}{Z}\langle R_n^2\rangle + \frac{3}{4}\left(\frac{\hbar}{M_p c}\right)^2$$
$$= \langle r^2\rangle_p + 0.769 - \frac{N}{Z}0.1161 + 0.033, \quad (7)$$

where $r_{\rm p}$ is the radius of point proton distribution of a nucleus, $R_{\rm p}$ and $R_{\rm n}$ are the charge radii of free proton and free neutron, respectively, and the last term is the so called Darwin-Foldy term (0.033 fm$^2$).

The root mean square (rms) charge radius $R_c = \sqrt{\langle r_c^2\rangle}$.

## III. RESULTS AND DISCUSSION

Shell model calculations are performed with NuShellX@MSU [25] to get the OBDM elements and energy levels. NuShellX@MSU is a set of wrapper codes written by A. Brown that use data files for model spaces and Hamiltonians to generate input for NuShellX [26]. It uses a $J$-coupled proton-neutron basis, and $J$-scheme matrix dimensions of up to the order of 100 million can be considered. In the present work, calculations are performed with $sdpf$ model space with valence (active) protons restricted to the $sd$ shell and $N-20$ valence neutrons to the $pf$ shell. The 20 neutrons are frozen in $s$, $p$, and $sd$ shells (full $sd$ valence space for $Z-8$ protons and full $fp$ valence space for $N-20$ neutrons). Results are based on the $sdpf$ interaction $sdpf$-$u$ [27].

The radial wave functions for the single-particle matrix elements are calculated with the harmonic oscillator potential with size parameters $b_{\rm c}$ adjusted to reproduce the measured rms charge radius of Ref. [28]. For nuclei for which no practical measurements of rms charge radius are available, the size parameter $b$ is obtained from a global formula for the oscillator length, which gives a smooth two parameter fit to rms charge radii over the entire periodic table [29]:

$$b = \sqrt{\frac{\hbar}{m_p\omega}} = \frac{\hbar c}{\sqrt{m_p c^2\hbar\omega}},$$
$$\text{with } \hbar\omega = 45A^{-1/3} - 25A^{-2/3},$$

where $m_p$ is the proton mass.

The available measured rms charge radii ($R_C$) with the corresponding size parameters $b_c$ and the size parameters $b$ calculated from the global formula with the corresponding rms charge radii ($R_b$) are given in Table I.

Microscopic perturbed calculations have been performed to include configurations excluded by the MS which incorporate one-particle-one-hole excitation from the core and the MS orbits into all higher orbits with $2\hbar\omega$ excitations. Calculations for the magnetic moments for *sd-pf* cross-shell isotopes that have experimental values in Ref. [30] are presented. Effective nucleon $g$ factors $g_n^\ell = 0.0$ and $g_n^s = -3.19$ evaluated for the $fp$ shell were chosen for the neutrons [31], because of their best fit to the ground state $g$ factor of $^{41}$Ca. For the $sd$ protons, $g_p^\ell = 1.06$ and $g_p^s = 5.055$, adjusted to fit the ground state $g$ factor of $^{39}$K in a simple $(\pi d^{-1})_{3/2}$ configuration were used. For $^{39}$K, the experimental magnetic moment [+0.391 47(3) $\mu_N$] is reproduced exactly with $sd$ model space and USDA interaction [13] (new "universal" $sd$ (USD) Hamiltonian based on an updated set of binding energies and energy levels) using the above nucleon effective $g$ factors. $Q$ moments for those isotopes are also calculated. Calculation of $Q$ moments for $N = 28$ isotones is discussed. Evidence on the coupling of the particle motion to the high-frequency quadrupole modes was provided by the $E2$ effective charge for low-energy transitions by Bohr and Mottelson [3]. They formulated an expression for the effective charges to explicitly include neutron excess via

$$e^{\rm eff}(t_z) = e\,(t_z) + e\delta\, e(t_z),$$
$$\delta\, e(t_z) = Z/A - 0.32(N-Z)/A - 2t_z[0.32 - 0.3(N-Z)/A].$$

Calculations of $Q$ moments are also presented using these effective charges ($Q_{\rm BM}$) for a comparison.

TABLE I. Size parameters of the HO potential and rms charge radii. $R_C$ is the measured rms charge radius [28] and $b_c$ is the corresponding size parameter. The size parameter $b$ is calculated from the global formula [29] and $R_b$ is the corresponding rms charge radius.

| Nucleus | $N$ | g.s. ($J^\pi$) | $R_C$ (fm) | $b_c$ (fm) | $b$ (fm) | $R_b$ (fm) |
|---|---|---|---|---|---|---|
| $^{34}$Al | 21 | $4^-$ | | | 1.899 | 3.234 |
| $^{35}$Si | 21 | $7/2^-$ | | | 1.906 | 3.279 |
| $^{38}$S | 22 | $0^+$ | | | 1.927 | 3.365 |
| $^{40}$S | 24 | $0^+$ | | | 1.941 | 3.384 |
| $^{43}$S | 27 | $7/2^-$ | | | 1.960 | 3.413 |
| $^{38}$Cl | 21 | $2^-$ | | | 1.927 | 3.387 |
| $^{44}$Cl | 27 | $2^-$ | | | 1.966 | 3.445 |
| $^{39}$Ar | 21 | $7/2^-$ | 3.409 | 1.929 | 1.934 | 3.418 |
| $^{40}$Ar | 22 | $0^+$ | 3.427 | 1.940 | 1.941 | 3.428 |
| $^{41}$Ar | 23 | $7/2^-$ | 3.425 | 1.940 | 1.947 | 3.437 |
| $^{43}$Ar | 25 | $5/2^-$ | 3.441 | 1.951 | 1.960 | 3.456 |
| $^{40}$K | 21 | $4^-$ | 3.438 | 1.936 | 1.941 | 3.446 |
| $^{41}$K | 22 | $3/2^+$ | 3.452 | 1.945 | 1.947 | 3.455 |
| $^{42}$K | 23 | $2^-$ | 3.452 | 1.945 | 1.953 | 3.465 |
| $^{43}$K | 24 | $3/2^+$ | 3.456 | 1.948 | 1.960 | 3.475 |
| $^{44}$K | 25 | $2^-$ | 3.456 | 1.949 | 1.966 | 3.484 |
| $^{45}$K | 26 | $3/2^+$ | 3.461 | 1.952 | 1.972 | 3.493 |
| $^{46}$K | 27 | $2^-$ | 3.456 | 1.950 | 1.978 | 3.502 |
| $^{47}$K | 28 | $1/2^+$ | 3.453 | 1.949 | 1.983 | 3.511 |
| $^{49}$K | 30 | $1/2^+$ | | | 1.995 | 3.529 |
| $^{51}$K | 32 | $3/2^+$ | | | 2.006 | 3.545 |

### A. Magnetic dipole moment

Magnetic dipole moments are calculated for *sd-pf* cross-shell isotopes that have experimental values in Ref. [30], $^{34}$Al(4$^-$), $^{35}$Si(7/2$^-$), $^{38}$S(2$^+$), $^{40}$S(2$^+$), $^{43}$S(7/2$^-$), $^{38}$Cl(2$^-$), $^{44}$Cl(2$^-$), $^{39}$Ar(7/2$^-$), $^{40}$Ar(2$^+$), $^{41}$Ar(7/2$^-$), $^{43}$Ar(5/2$^-$), $^{40}$K(4$^-$), $^{41}$K(3/2$^+$), $^{42}$K(2$^-$), $^{43}$K(3/2$^+$), $^{44}$K(2$^-$), $^{45}$K(3/2$^+$), $^{46}$K(2$^-$), $^{47}$K(1/2$^+$), $^{49}$K(1/2$^+$), and $^{51}$K(3/2$^+$). Free and effective nucleon $g(g_1)$ factors $g_{\rm p}^\ell = 1.06, g_{\rm p}^s = 5.055, g_{\rm n}^\ell = 0.0$, and $g_{\rm n}^s = -3.19$ are used. The results for the excited state energies and the magnetic moments are presented in Table II in comparison with the experimental data of Ref. [30].

TABLE II. Calculated and measured magnetic moments for *sd-pf* cross-shell nuclei according to the configurations $\pi[(sp)^8(sd)^{z-12}]\nu[(spsd)^{20}(pf)^{N-20}]$ using *sdpf-u* [27] interaction in comparison with available experimental values.

| Nucleus | $N$ | $J^\pi$ | Ex (MeV) Theory | Ex (MeV) Experiment | $\mu$ ($\mu_N$) Theory[a] | $\mu$ ($\mu$N) Theory[b] | $\mu$ ($\mu_N$) Experiment |
|---|---|---|---|---|---|---|---|
| $^{34}$Al | 21 | $4^-$ | 0 | 0 | 1.592 | 1.743 | (+)2.156(16) |
| $^{35}$Si | 21 | $7/2^-$ | 0 | 0 | − 1.476 | −1.188 | (−)1.638(4) |
| | | | | | | − 1.660[c] | |
| $^{38}$S | 22 | $2^+$ | 1.459 | 1.292 | − .011 | 0.103 | +0.26(10) |
| $^{40}$S | 24 | $2^+$ | 0.942 | 0.904 | 0.055 | 0.156 | |
| | | | | | | − 0.027[c] | − 0.02(12) |
| $^{43}$S | 27 | $7/2^-$ | 0.262 | 0.320 | − 0.549 | − 0.268 | 1.110(14) |
| | | | | | − 1.205[d] | − .816[e] | |
| $^{38}$Cl | 21 | $2^-$ | 0 | 0 | − 2.042 | − 1.893 | 2.05(2) |
| $^{44}$Cl | 27 | $2^-$ | 0 | 0 | − 0.165 | − 0.158 | (−)0.275(2) |
| $^{39}$Ar | 21 | $7/2^-$ | 0 | 0 | − 1.756 | − 1.433 | − 1.588(15) |
| $^{40}$Ar | 22 | $2^+$ | 1.281 | 1.461 | − 0.456 | − 0.269 | − 0.04(6) |
| $^{41}$Ar | 23 | $7/2^-$ | 0 | 0 | − 1.342 | − 1.072 | − 1.309(8) |
| $^{43}$Ar | 25 | $5/2^-$ | 0 | 0 | − 0.930 | − 0.741 | − 1.021(6) |
| $^{40}$K | 21 | $4^-$ | 0 | 0 | − 1.778 | − 1.330 | − 1.298 (3) |
| $^{41}$K | 22 | $3/2^+$ | 0 | 0 | − 0.096 | 0.153 | +0.2148701(2) |
| $^{42}$K | 23 | $2^-$ | 0 | 0 | − 1.345 | − 1.196 | − 1.1425(6) |
| $^{43}$K | 24 | $3/2^+$ | 0 | 0 | − 0.229 | 0.0145 | +0.1633(8) |
| | | | | | | 0.167[c] | |
| $^{44}$K | 25 | $2^-$ | 0 | 0 | − 0.431 | − 0.422 | − 0.856(4) |
| $^{45}$K | 26 | $3/2^+$ | 0 | 0 | − 0.189 | 0.050 | +0.1734(8) |
| | | | | | | 0.206[c] | |
| $^{46}$K | 27 | $2^-$ | 0 | 0 | − 0.553 | − 0.584 | − 1.051(6) |
| | | | | | | − 1.175[c] | |
| $^{47}$K | 28 | $1/2^+$ | 0 | 0 | 2.303 | 2.076 | +1.933(9) |
| $^{49}$K | 30 | $1/2^+$ | 0 | 0 | 2.195 | 1.981 | +1.3386(8) |
| $^{51}$K | 32 | $3/2^+$ | 0 | 0 | 0.200 | 0.431 | +0.513(2) |

[a]Free $g$ factors.
[b]Effective $g_1$ factors $g_p^\ell = 1.06$, $g_p^s = 5.055$, $g_n^\ell = 0.0$ and $g_n^s = -3.19$.
[c]Effective $g_2$ factors $g_p^\ell = 1.15$, $g_p^s = 4.748$, $g_n^\ell = -0.15$ and $g_n^s = -3.252$.
[d]$(1f_{7/2}\,2p_{3/2})^7$ configuration with free nucleon $g$ factors.
[e]$(1f_{7/2}\,2p_{3/2})^7$ configuration with effective nucleon $g_2$ factors.

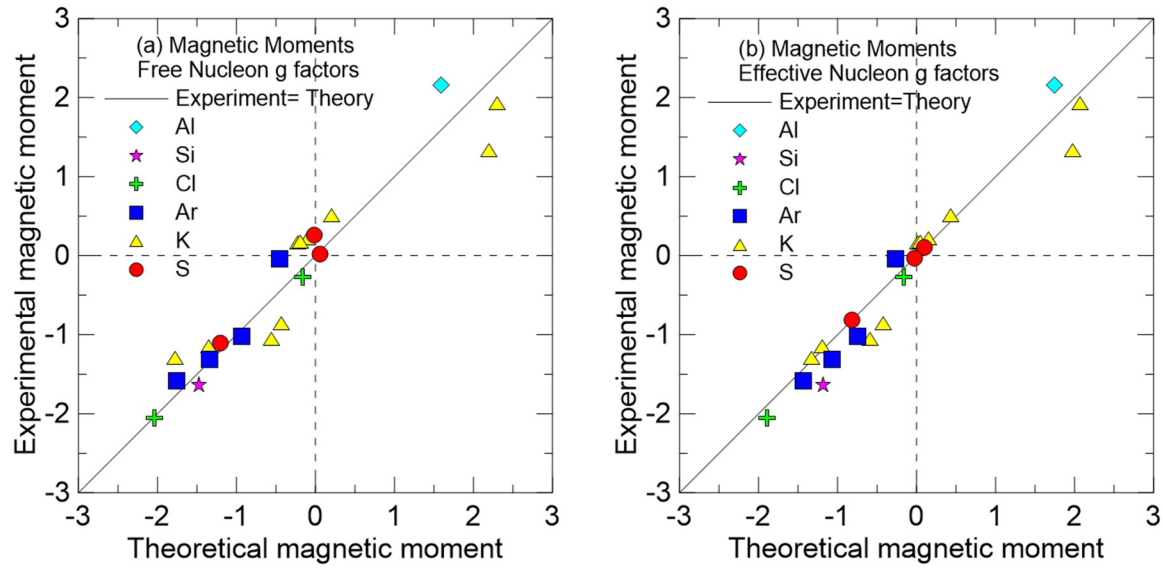


FIG. 1. Comparison between the experimental and theoretical magnetic moments $\mu$, using free $g$ factors (a) and effective $g$ factors (b). The experimental values are taken from Ref. [30].

TABLE III. Calculated and measured $g$ factors in comparison with those of the collective values.

| Nucleus | $N$ | $J^\pi$ | $g = \lvert\mu/J\rvert$ | $g \sim Z/A$ | $g_{\rm exp}$ |
|---|---|---|---|---|---|
| | | **$_{13}$Al** | | | |
| $^{34}$Al | 21 | $4^-$ | 0.40 | 0.38 | 0.539 |
| | | **$_{14}$Si** | | | |
| $^{35}$Si | 21 | $7/2^-$ | 0.42 | 0.4 | 0.43 |
| | | **$_{16}$S** | | | |
| $^{38}$S | 22 | $2^+$ | 0.01 | 0.42 | 0.13 |
| $^{40}$S | 24 | $2^+$ | 0.03 | 0.4 | 0.01 |
| $^{43}$S | 27 | $7/2^-$ | 0.16 | 0.37 | 0.32 |
| | | **$_{17}$Cl** | | | |
| $^{38}$Cl | 21 | $2^-$ | 1.02 | 0.45 | 1.03 |
| $^{44}$Cl | 27 | $2^-$ | 0.08 | 0.39 | 0.14 |
| | | **$_{18}$Ar** | | | |
| $^{39}$Ar | 21 | $7/2^-$ | 0.50 | 0.46 | 0.45 |
| $^{40}$Ar | 22 | $2^+$ | 0.23 | 0.45 | 0.02 |
| $^{41}$Ar | 23 | $7/2^-$ | 0.38 | 0.44 | 0.37 |
| $^{43}$Ar | 25 | $5/2^-$ | 0.37 | 0.42 | 0.41 |
| | | **$_{19}$K** | | | |
| $^{40}$K | 21 | $4^-$ | 0.44 | 0.47 | 0.32 |
| $^{41}$K | 22 | $3/2^+$ | 0.06 | 0.46 | 0.15 |
| $^{42}$K | 23 | $2^-$ | 0.67 | 0.45 | 0.77 |
| $^{43}$K | 24 | $3/2^+$ | 0.15 | 0.44 | 0.11 |
| $^{44}$K | 25 | $2^-$ | 0.22 | 0.43 | 0.43 |
| $^{45}$K | 26 | $3/2^+$ | 0.13 | 0.42 | 0.12 |
| $^{46}$K | 27 | $2^-$ | 0.28 | 0.41 | 0.53 |
| $^{47}$K | 28 | $1/2^+$ | 4.61 | 0.40 | 3.87 |
| $^{49}$K | 30 | $1/2^+$ | 4.39 | 0.39 | 2.68 |
| $^{51}$K | 32 | $3/2^+$ | 0.13 | 0.37 | 0.34 |

The calculated value for $^{34}$Al ($1.592\,\mu_N$) underestimates the measured value [$(+)\,2.156\,(16)\,\mu_N$] by about a factor of 1.3. The sign is correctly reproduced. The magnetic moment becomes $1.743\mu_N$ with the effective nucleon $g$ factors becoming closer to the measured value.

The calculated value for $^{35}$Si ($-1.476\mu_N$) is very close to the measured value [$(-)\,1.638(4)\,\mu_N$]. The sign is correctly reproduced. The magnetic moment becomes $-1.188\mu_N$ with the effective nucleon $g_1$ factors, which increases the discrepancy with the measured value. The experimental values for $^{49}$K and $^{51}$K [32] are compared to effective single-nucleon $g$ factors, with typical values for the $sd$ shell [33] [$g_{\rm p}^{\ell} = 1.15$, $g_{\rm p}^{s} = 0.85\, g_{\rm p}^{s}$(free), $g_{\rm n}^{\ell} = -0.15$ and $g_{\rm n}^{s} = 0.85\, g_{\rm n}^{s}$(free)]. Using these effective nucleon $g(g_2)$ factors, the experimental value of $^{35}$Si is very well reproduced, in sign and magnitude, $\mu = -1.660\mu_N$ in comparison to the measured value $-1.638(4)\mu_N$.

The measured magnetic moment for the excited $2^+$ state (1.292 MeV) of $^{38}$S[$+0.26(10)\mu_N$] is underpredicted by around an order of magnitude with an opposite sign. Effective nucleon $g_1$ factors result ($\mu = 0.103\mu_N$) predicts the correct sign and becomes close to the measured value, within the experimental error. However, the effective nucleon $g_2$ factors of Refs. [32,33] predict the value $-0.0775\mu_N$, which underpredicts the measured value and predicts the wrong sign. The calculated magnetic moment ($0.055\mu_N$) for $^{40}$S agrees with the measured value [$-0.02(12)\mu_N$], within the experimental errors, but with an opposite sign. Effective nucleon $g_1$ factors increase the value by about three times. So, this discrepancy is not resolved by these effective nucleon $g_1$ factors. Using the effective nucleon $g_2$ factors, the experimental value of $^{40}$S is

TABLE IV. Calculated $Q$ moments of neutron excess *sd-pf* cross-shell nuclei according to the configurations $\pi[(sp)^8(sd)^{z-12}]\nu[(spsd)^{20}(pf)^{N-20}]$ using $sdpfu$ interaction in comparison with available experimental values. Effective $C2$ charges presented are deduced from CP calculations at the photon points. Effective charges calculated with BM model and the corresponding $Q$ moments are also displayed.

| Nucleus | $N$ | $J^\pi$ | $Q(e\,{\rm fm}^2)$ Theory | CP Effective charges $e_{\rm p}$, $e_{\rm n}(e)$ | BM Effective charges $e_{\rm p}$, $e_{\rm n}(e)$ | $Q_{\rm BM}(e\,{\rm fm}^2)$ | $Q(e\,{\rm fm}^2)$ Experiment |
|---|---|---|---|---|---|---|---|
| $^{34}$Al | 21 | $4^-$ | − 2.25 | 1.20, 0.37 | 1.06, 0.56 | − 2.50 | |
| $^{35}$Si | 21 | $7/2^-$ | − 11.06 | 1.28, 0.28 | 1.08, 0.60 | − 12.92 | |
| $^{38}$S | 22 | $2^+$ | − 7.00 | 1.33, 0.32 | 1.10, 0.64 | − 8.64 | |
| $^{40}$S | 24 | $2^+$ | − 14.18 | 1.24, 0.34 | 1.08, 0.60 | − 17.05 | |
| $^{43}$S | 27 | $7/2^-$ | − 20.26 | 1.25, 0.37 | 1.05, 0.53 | − 21.85 | 23(3) |
| $^{38}$Cl | 21 | $2^-$ | − 6.17 | 1.23, 0.29 | 1.13, 0.70 | − 8.47 | |
| $^{44}$Cl | 27 | $2^-$ | 11.71 | 1.30, 0.30 | 1.06, 0.57 | 13.10 | |
| $^{39}$Ar | 21 | $7/2^-$ | − 11.72 | 1.31, 0.25 | 1.14, 0.73 | − 15.57 | −12(2) |
| $^{40}$Ar | 22 | $2^+$ | 6.82 | 1.05, 0.53 | 1.13, 0.71 | 7.77 | +1(4) |
| $^{41}$Ar | 23 | $7/2^-$ | − 3.64 | 1.26, 0.33 | 1.12, 0.68 | − 4.72 | −4.2(4) |
| $^{43}$Ar | 25 | $5/2^-$ | 8.71 | 1.18, 0.35 | 1.10, 0.64 | 13.10 | 14.2(14) |
| $^{40}$K | 21 | $4^-$ | − 6.37 | 1.18, 0.31 | 1.15, 0.76 | − 10.07 | −7.3(1) |
| $^{41}$K | 22 | $3/2^+$ | 6.85 | 1.36, 0.23 | 1.14, 0.74 | 8.89 | +7.11(7) |
| $^{42}$K | 23 | $2^-$ | − 6.04 | 1.15, 0.33 | 1.13, 0.71 | − 10.38 | |
| $^{43}$K | 24 | $3/2^+$ | 7.38 | 1.24, 0.32 | 1.12, 0.69 | 9.88 | |
| $^{44}$K | 25 | $2^-$ | − 2.40 | 1.14, 0.34 | 1.11, 0.67 | − 4.27 | |
| $^{45}$K | 26 | $3/2^+$ | 7.79 | 1.26, 0.34 | 1.10, 0.65 | 9.71 | |
| $^{46}$K | 27 | $2^-$ | 5.57 | 1.19, 0.36 | 1.09, 0.63 | 7.83 | |
| $^{51}$K | 32 | $3/2^+$ | 8.35 | 0.94, 0.83 | 1.05, 0.53 | 7.63 | |

TABLE V. Calculated $Q$ moments of neutron excess *sd-pf* cross-shell nuclei with $N = 28$ and $J^\pi = 2^+$ according to the configurations $\pi[(sp)^8(sd)^{z-12}]\nu[(spsd)^{20}(pf)^8]$ using $sdpfu$ interaction. Effective $C2$ charges presented are deduced from CP calculations at the photon points. Effective charges calculated with BM model and the corresponding $Q$ moments are also displayed.

| Nucleus | Ex (MeV) Theory | Ex (MeV) Experiment | $Q(e\,\mathrm{fm}^2)$ Theory | Effective charges $e_p$, $e_n(e)$ | BM effective charges | $Q_{BM}(e\,\mathrm{fm}^2)$ |
|---|---|---|---|---|---|---|
| $^{42}$Si | 1.123 | 0.77 | 17.72 | 1.28, 0.35 | 1.01, 0.45 | 16.97 |
| $^{44}$S | 1.172 | 1.315 | − 15.84 | 1.25, 0.38 | 1.04, 0.51 | − 16.43 |
| $^{46}$Ar | 1.594 | 1.550 | 16.66 | 1.39, 0.26 | 1.07, 0.58 | 17.97 |
| $^{48}$Ca | 4.816 | 3.831 | 2.34 | 1.11, 0.29 | 1.09, 0.63 | 5.12 |

very well reproduced, in sign and magnitude, $\mu = -0.027\mu_N$ in comparison to the measured value $-0.02(12)\mu_N$. The experimental magnetic moment for the first excited state $7/2^-$ of $^{43}$S [1.11(14)$\mu_N$] is underestimated by about a factor of 2. The sign of the experimental value is undetermined, and our calculation predicts a negative sign. Calculations with effective nucleon $g_1$ factors give the value of the magnetic moment $-0.268\mu_N$ which underestimates the measured value by about a factor of 4. The configuration $(1f_{7/2})^{-1}$ fails also to predict $\mu$ for this isotope. Stuchbery *et al.* [34] showed that the magnetic moment is extremely sensitive to the occupation of the neutron $p_{3/2}$ orbit above the $N = 28$ shell gap for $^{38}$S and $^{40}$S. Using the configuration $(1f_{7/2}\,2p_{3/2})^7$, the magnetic moment becomes $-1.2\mu_N$, in comparison with the measured value $1.110(14)\mu_N$ (sign is not determined), with 94% occupation for $1f_{7/2}$ and 6% for $2p_{3/2}$. Effective $g_1$ factors give the value $0.816\mu_N$, while those of $g_2$ give the value $-1.128\mu_N$, which reproduces the experimental value.

The experimental value of the Chlorine isotopes $^{38}$Cl and $^{44}$Cl is well reproduced with free nucleon $g$ factors. The small reduction in the values of $\mu$ with effective nucleon $g_1$ factors still agrees with the experimental value within its error. The calculations predict a negative sign.

The measured magnetic moment for the ground state of $^{39}$Ar [$-1.588(15)\mu_N$], $^{41}$Ar [$1.309(8)\mu_N$] and $^{43}$Ar [$-1.021(6)\mu_N$] are very well reproduced by the shell model calculation with free nucleon $g$ factors ($-1.756$, $-1.342$, and $-0.930\mu_N$, respectively). Small reductions in the values of $\mu$ with effective nucleon $g_1$ factors are still close to the experimental values. Calculations predict a negative sign as the measured values. The calculated magnetic moment for $^{40}$Ar ($-0.456\mu_N$) overestimates the measured value [$-0.04(6)\mu_N$]. Using effective nucleon $g_1$ factors, the magnetic moment becomes $-0.269\mu_N$ which reduces the discrepancy between theory and experiment but does not eliminate it. The shell model code is optimized for spectroscopic properties, but not necessarily for the nuclear charge, convection, and magnetization current densities.

The measured magnetic moment for the ground state of $^{40}$K [$-1.298(3)\mu_N$], $^{41}$K [$+0.214\,870\,1(2)\mu_N$], $^{42}$K [$-1.1425(6)\mu_N$], $^{44}$K[$-0.856(4)\mu_N$, $^{47}$K[$+1.933(9)\mu_N$], $^{49}$K [$+1.3386(8)\mu_N$], and $^{51}$K [$+0.513(2)\mu_N$] are well described by effective nucleon $g_1$ factors, and predict the correct signs. For $^{43}$K, the value of the measured magnetic moment is underestimated by about a factor of 1.4. The calculation predicts the wrong sign. Effective nucleon $g_1$ factors give the correct sign, but underestimate the measured value by an order of magnitude. Using the effective nucleon $g_2$ factors, the magnetic moment becomes $0.167\mu_N$, which reproduces the measured value [$0.1633(8)\mu_N$] in sign and magnitude. For $^{45}$K, the value of the measured magnetic moment is well reproduced by magnitude, but with opposite

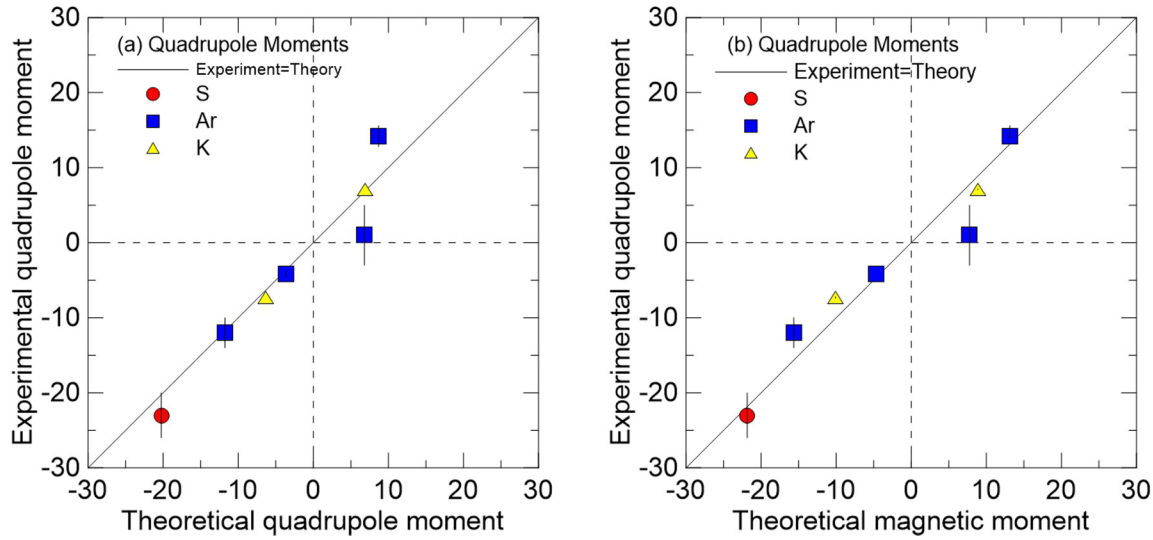


FIG. 2. Quadrupole moments for Ar, K, and S isotopes calculated with CP (a) and with BM effective charges (b) in comparison with the experimental values of Ref. [30].

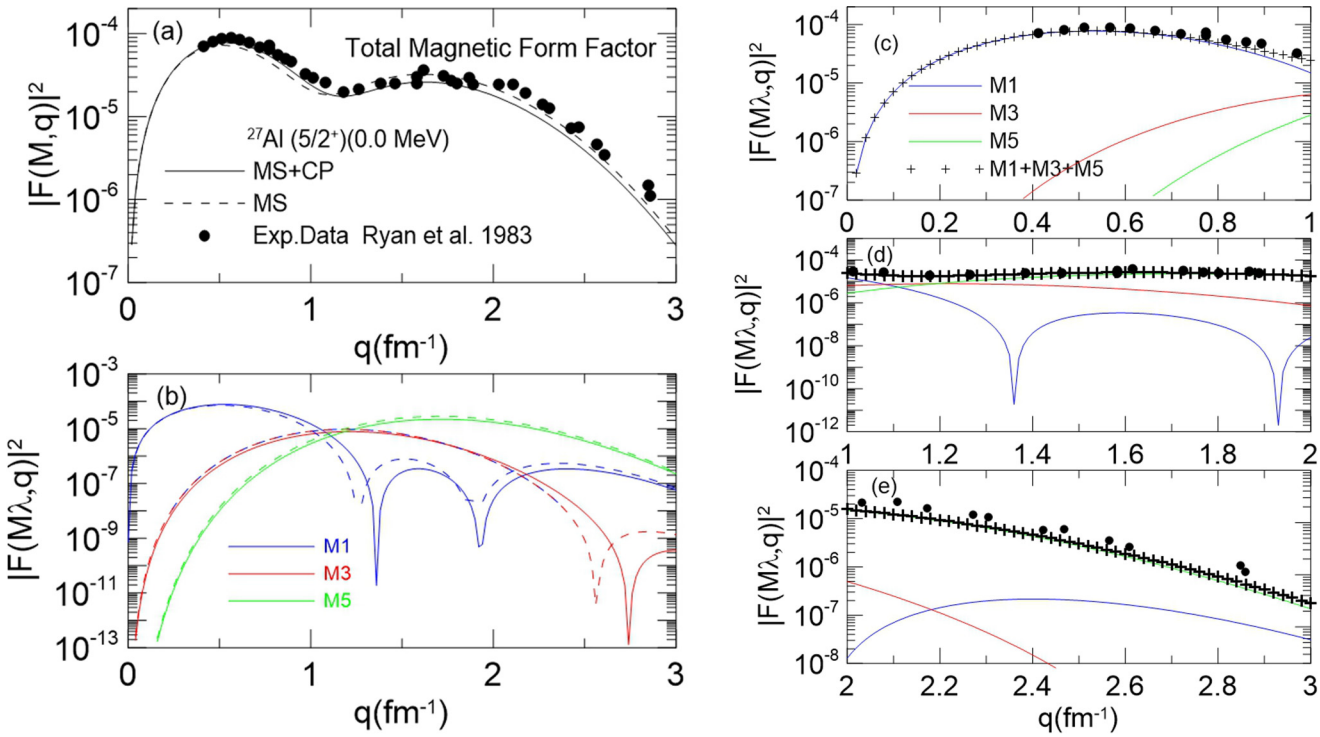


FIG. 3. Total elastic magnetic form factors for $^{27}$Al (a). The contribution of each multipole is shown in (b). The solid curves are with CP and the dashed curve with MS only. The data are taken from Ryan *et al.* [38]. The right panel (c) shows the multipole contributions at different ranges of $q$.

sign. Effective nucleon $g_1$ factors give the correct sign, but underestimate the measured value by about a factor of 3. Effective nucleon $g_2$ factors predict the correct sign and give the value $0.206\mu_N$ which is close to the measured value $+0.1734(8)\mu_N$. For $^{46}$K, the value of the measured magnetic moment is underestimated by about a factor of 2, with the correct negative sign. Effective nucleon $g_1$ factors have a little effect on this value. Effective nucleon $g_2$ factors eliminate the discrepancy and predict the value $-1.175\mu_N$ which is very close to the measured value $-1.051(6)\mu_N$. The calculated magnetic moments using free nucleon $g$ factors and effective nucleon $g$ factors are presented in Figs. 1(a) and 1(b), respectively in comparison with the measured values of Ref. [30].

The collective model expectations of $g \sim Z/A$ for the above isotopes are tabulated in Table III in comparison with our calculations, using free $g$ factors. Some of the isotopes discussed above show collective features, while other isotopes do not show these features.

### B. Quadrupole moments

Quadrupole moments for the isotopes discussed in Sec. III A are also calculated. Calculations are also presented for $N = 28$ isotones. These calculations include CP and BM effective charges. The results for the excited state energy and the $Q$ moments are presented in Table IV in comparison with the available experimental data of Ref. [30]. These values are close to each other and predict a small oblate deformation for $^{34}$Al. The occupation number for the $1d_{5/2}$ orbit is 4.7 out of 5 (94%). One valence neutron with more than 80% probability is in $1f_{7/2}$. So, coupling of the dominant proton hole in $1d_{5/2}$ with the dominant neutron in $1f_{7/2}$ continue the spherical shape of this nucleus.

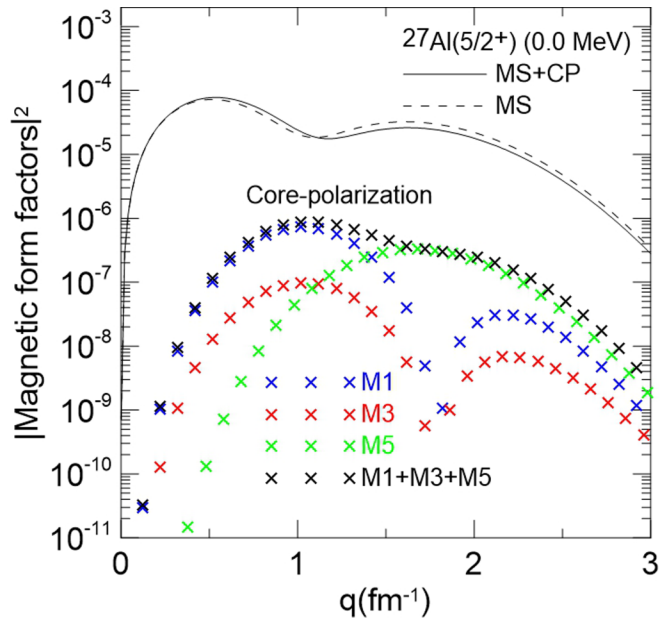


FIG. 4. Elastic magnetic form factors for $^{27}$Al. The CP contribution of different multipoles are denoted by the cross symbols. Model space magnetic form factor and that including CP are denoted by the dashed and solid curves, respectively.

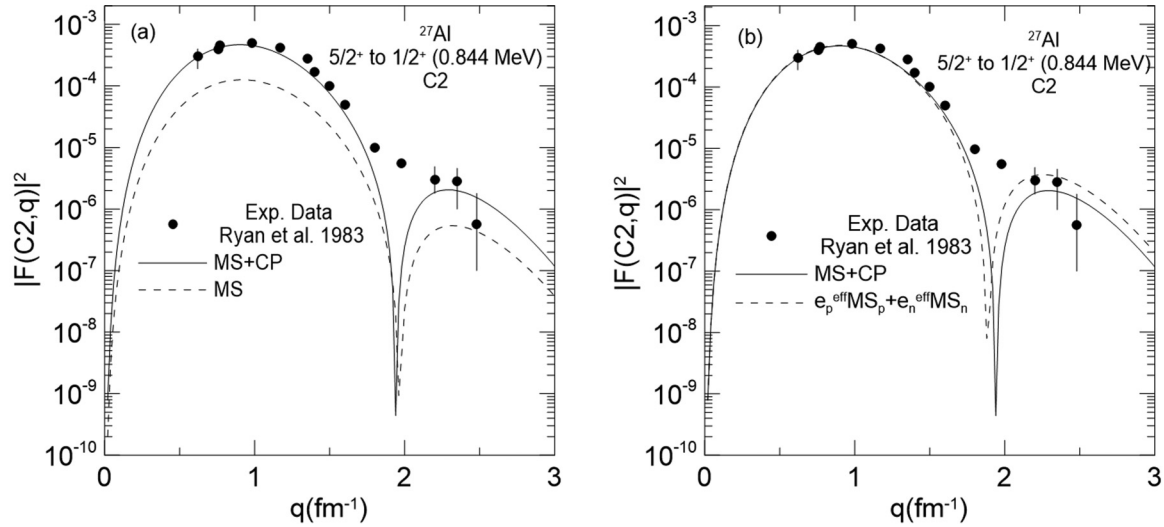


FIG. 5. Longitudinal C2 form factor for the $1/2^+$ (0.844 MeV) state in $^{27}$Al, calculated with MS (dashed curve) in comparison with that including CP effect (solid curve) (a). The right panel (b) shows a comparison of the calculated C2 form factors using CP effect (solid curve) with that of the effective charge model (dashed curve). The experimental data are taken from Ryan *et al.* [38].

The results for $^{35}$Si are $-11.06\,e\,\mathrm{fm}^2$ and $-12.92\,e\,\mathrm{fm}^2$ calculated with CP and BM effective charges, respectively. These values are close to each other and predict a large oblate deformation. The valence protons mostly filled the $1d_{5/2}$ orbit by about 93%. One valence neutron with more than 99% probability is in $1f_{7/2}$. So, the $Q$ moment is due to that unpaired neutron and explains the large oblate deformation.

The results for $^{38}$Si are $-7.00\,e\,\mathrm{fm}^2$ and $-8.64\,e\,\mathrm{fm}^2$ calculated with CP and BM effective charges, respectively. These values predict an oblate deformation. So a development of collective feature in this neutron-rich isotope occurs [31] in comparison with $^{36}$S ($N = 20$). Since no measured value of the $Q$ moment, we can check our calculation with the measured $B(E2)$ value ($0^+$ to $2^+_1$) of Ref. [35] $230 \pm 30\,e^2\,\mathrm{fm}^4$ which is very well reproduced by BM effective charges, $236\,e^2\,\mathrm{fm}^4$. We believe that the $Q$ moment is well reproduced by the full $\pi(sd)^{-2}$ and full $\nu(fp)^2$ model spaces with CP and BM effective charges. The results for $^{40}$S are $-14.18\,e\,\mathrm{fm}^2$ and $-17.05e\,\mathrm{fm}^2$ calculated with CP and BM effective charges, respectively. These values predict an oblate deformation. The experimental value of $^{43}$S is well explained with both CP and BM effective charges within the experimental error.

The experimental value of $^{39}$Ar is well reproduced by the CP calculation, and is overpredicted by the BM model. For $^{40}$Ar, the measured $Q$ moment $[+1(4)\,e\,\mathrm{fm}^2]$ is underestimated. The quadrupole moment as well as the magnetic moment for the $2^+$ state of $^{40}$Ar cannot be explained by the model considered in this work, even though the measured excitation energy 1.281 MeV is well reproduced (1.461 MeV). For $^{41}$Ar, both calculations are close to the measured value within the experimental error. For $^{43}$Ar, the experimental value $[14.2(14)\,e\,\mathrm{fm}^2]$ is well reproduced by the BM model ($13.12\,e\,\mathrm{fm}^2$), while it is underestimated by about a factor of 1.5 with CP calculation. This isotope is with $N = 25$. Enhanced collectivity at $N = 25$ may reduce the $N = 28$ shell gap [36] for this large neutron excess isotope, which gives a high quadrupole moment, which is well described by the collective model with the BM effective charges. The $Q$ moments for $^{40}$K and $^{41}$K are well explained by both calculations.

The core-polarization effect enhances the $Q$ moments for the above isotopes by about a factor of 1.3–2.

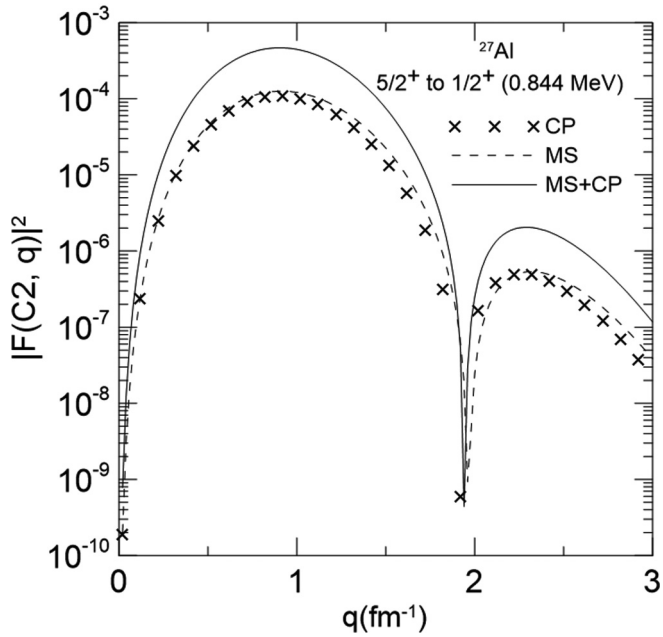


FIG. 6. Longitudinal $C2$ form factors for $^{27}$Al. The CP contribution is denoted by the cross symbols. Model space and total $C2$ form factors are denoted by the dashed and solid curves, respectively. Elastic magnetic and longitudinal $C2$ form factors are calculated including CP effects for one isotope of each neutron-rich nucleus considered in this work. The results are shown in Figs. 7–12, for $^{34}$Al, $^{35}$Si, $^{43}$S, $^{38}$Cl, $^{39}$Ar, and $^{40}$K. Small suppression of the magnetic form factors is noticed with CP effects. Enhancement of the form factor is noticed with the inclusion of CP effects for the longitudinal C2 form factors for the first lope and a suppression occurs in the form factors for the second lope, for $q \geqslant 2.5\,\mathrm{fm}^{-1}$.

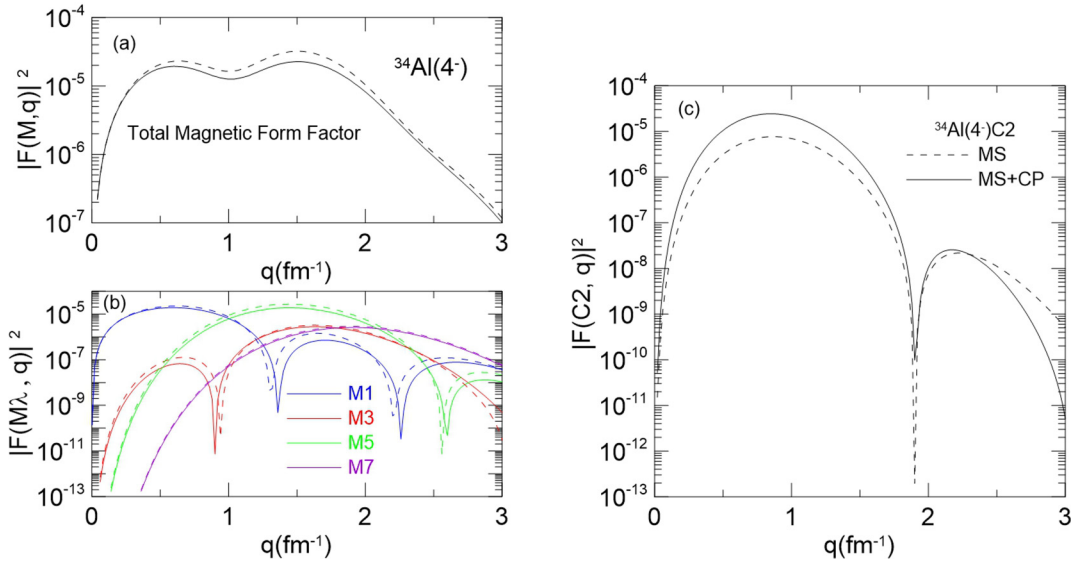


FIG. 7. Elastic magnetic form factors (a) with the contribution of the different multipolarities (b) and $C2$ longitudinal form factor (c) for $4^-$ ground state of $^{34}$Al. Dashed curves represent the MS form factors and the solid curves represent the MS + CP form factors.

The isotones $^{42}$Si, $^{44}$S, and $^{46}$Ar are with $N = 28$. The $Q$ moments calculated with CP are 17.72, −15.84, and 16.66$e$ fm$^2$ and with BM effective nucleon charges are 16.97, −16.43, and 17.97$e$ fm$^2$ for the $J^\pi = 2^+$ of the above isotones, respectively. These values of both calculations are close to those of Ref. [37] (calculated with different effective charges). Another isotone is $^{48}$Ca, where it is known as a doubly magic nucleus. The calculated $Q$ moment with CP effect is 2.35$e$ fm$^2$. This small value predicts small deformation, nearly spherical. If two protons or more are removed from $Z = 20$, the $Q$ moments increase appreciably and the isotones $^{42}$Si, $^{44}$S, and $^{46}$Ar become more deformed by going toward the neutron drip line even though the neutron number is a magic number. The values of the $Q$ moments for these isotones are tabulated in Table V.

The values of the calculated and measured $Q$ moments are displayed in Fig. 2.

### C. Elastic magnetic and $C2$ longitudinal form factors

Elastic magnetic and longitudinal form factors are calculated for the ground state for one isotope of each nucleus.

Before calculating the form factors for the neuron rich cross-shell nuclei where no experimental data are available, we first calculate the elastic magnetic form factors for the ground state $(5/2^+)$ of $^{27}$Al nucleus and the $C2$ longitudinal form factor for the $1/2^+(0.844\,\text{MeV})$ state and compare those with the experimental data. For $^{27}$Al, the $sd$-shell model space is adopted with the interaction USDA [13].

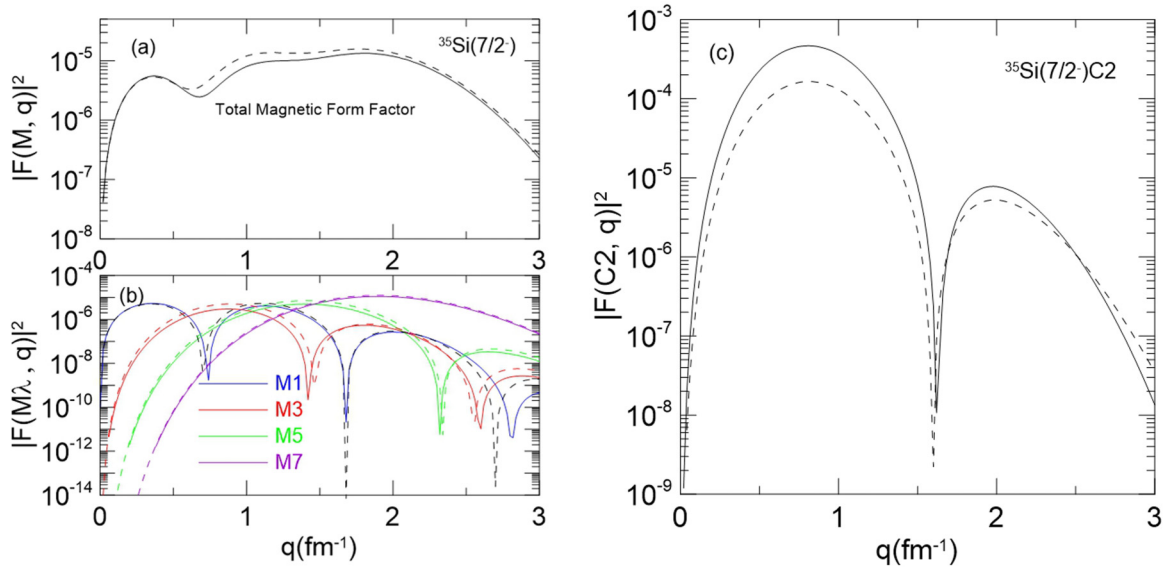


FIG. 8. Elastic magnetic form factors (a) with the contribution of the different multipolarities (b) and $C2$ longitudinal form factor (c) for $7/2^-$ ground state of $^{35}$Si. Dashed curves represent the MS form factors and the solid curves represent the MS + CP form factors.

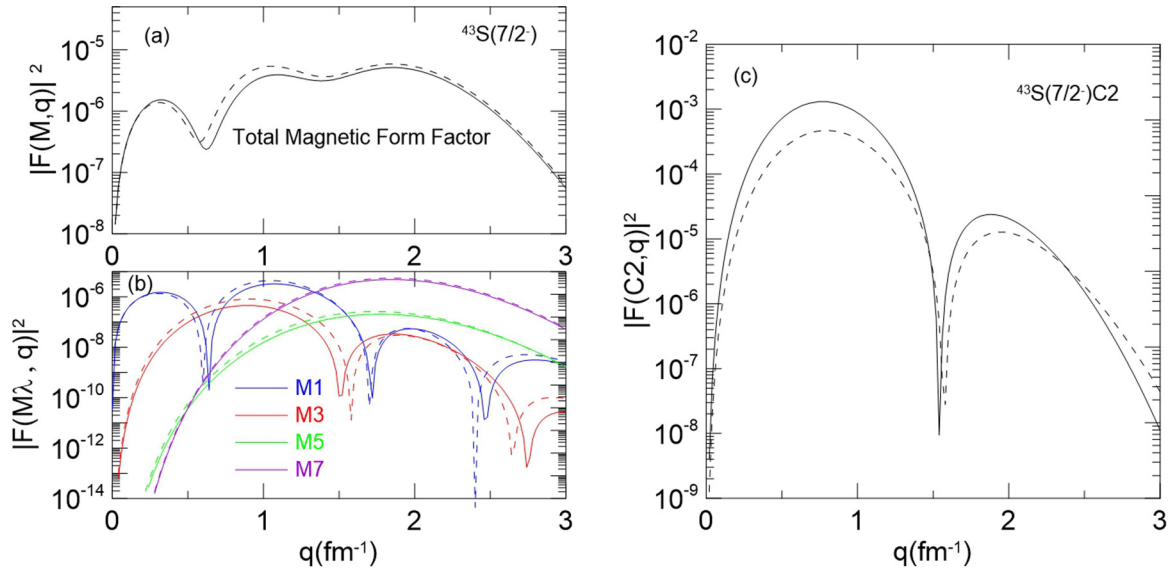


FIG. 9. Elastic magnetic form factors (a) with the contribution of the different multipolarities (b) and $C2$ longitudinal form factor (c) for $7/2^-$ ground state of $^{43}$S. Dashed curves represent the MS form factors and the solid curves represent the MS + CP form factors.

Elastic magnetic form factors are calculated with $b = 1.784$ fm, chosen to reproduce the rms charge radius, 3.061 fm [28]. The calculated magnetic moment is $3.479\mu_N$ which is very close to the experimental value $+3.642(7)\mu_N$. The calculated $Q$ moment including CP is $14.08\,e\,\mathrm{fm}^2$ which is close to the experimental value $Q_{\mathrm{exp}} = 14.66(10)\,e\,\mathrm{fm}^2$. The calculated effective charges in this case are $e_{\mathrm{p}} = 1.2\,e$, $e_{\mathrm{n}} = 0.5e$. The calculated $Q$ moment using the BM effective charges $e_{\mathrm{p}} = 1.16\,e$, $e_{\mathrm{n}} = 0.78\,e$ is $Q = 15.32\,e\,\mathrm{fm}^2$, which is also close to the measured value.

Elastic magnetic form factors for $^{27}$Al are displayed in Fig. 3 calculated by including CP (solid curves) and without CP, i.e., with the MS only (dashed curves). A small enhancement is noticed for $M1$ for $q < 1.2\,\mathrm{fm}^{-1}$ and a very small suppression for $q > 1.2\,\mathrm{fm}^{-1}$, and the minimum is shifted to larger $q$, by including CP. The data of Ref. [38] are very well reproduced. The contribution of each multipole is shown also in Fig. 3(b). Figure 3(c) shows the contribution of each of the three multipoles for $q$ between 0 and $1\,\mathrm{fm}^{-1}$. The total magnetic form factor in this region is almost totally $M1$, which explains the data very well. Figure 3(d) shows the contribution for $q$ between 1 and $2\,\mathrm{fm}^{-1}$. The total magnetic form factor in this region is almost totally $M5$, which explains the data very well. In the region of $q$ between 2 and $3\,\mathrm{fm}^{-1}(e)$, the total form factor is due to $M5$.

Core-polarization effects are shown for the different multipoles as a function of $q$ in Fig. 4. The effect of the CP ($2\hbar\omega$) contribution is very small in comparison with the MS

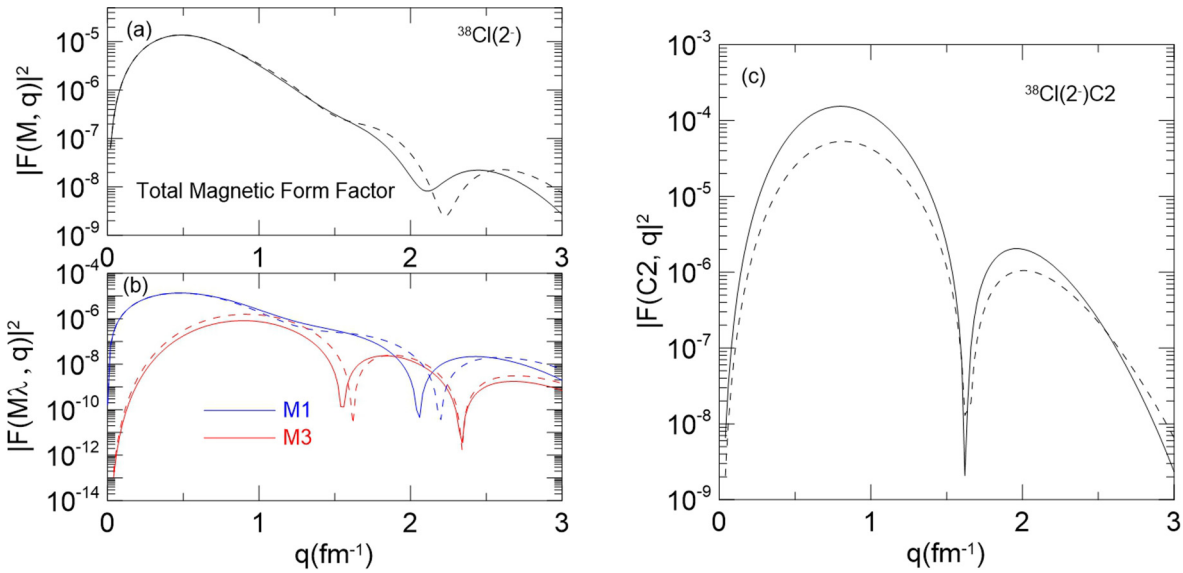


FIG. 10. Elastic magnetic form factors (a) with the contribution of the different multipolarities (b) and $C2$ longitudinal form factor (c) for $2^-$ ground state of $^{38}$Cl. Dashed curves represent the MS form factors and the solid curves represent the MS + CP form factors.

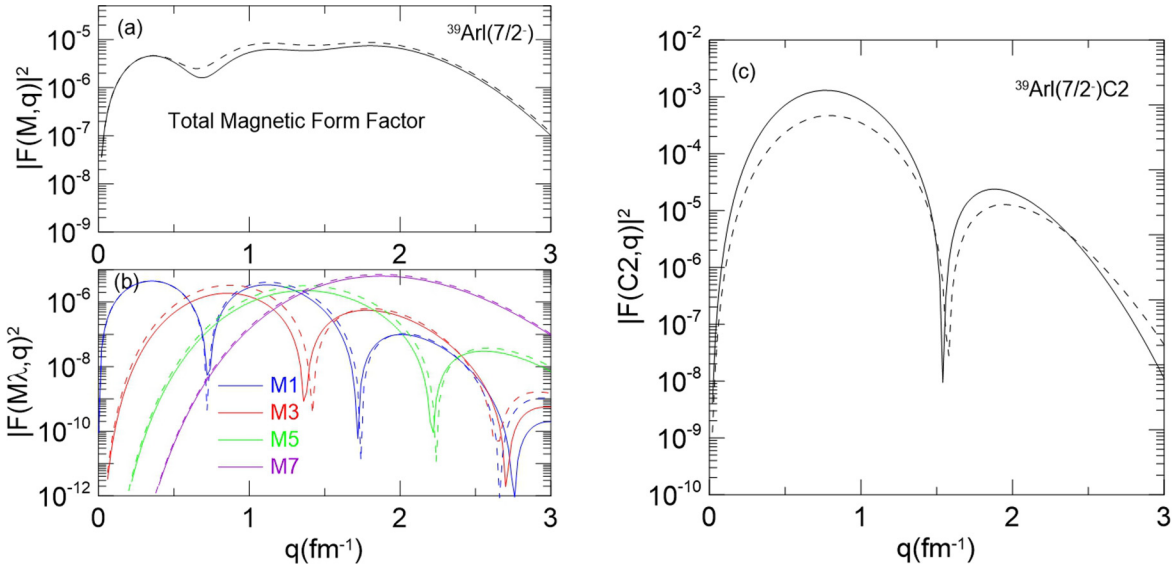


FIG. 11. Elastic magnetic form factors (a) with the contribution of the different multipolarities (b) and $C2$ longitudinal form factor (c) for $7/2^-$ ground state of $^{39}$Ar. Dashed curves represent the MS form factors and the solid curves represent the MS + CP form factors.

$(0\hbar\omega)$ contribution for all multipoles and for all $q$ values. For magnetic electron scattering, the form factor depends on the spin and orbital angular momenta, and according to the shell model, most of the nucleon spins and orbital momenta pair off to yield zero contribution [39]. The nuclear magnetism thus is determined by a few valence nucleons, with an almost negligible effect of CP. Due to Suzuki [40], the tensor part of the M3Y interaction has a destructive interference for $j = l + 1/2$, which reduces the magnetic form factors, while the other part leads to an increase of the magnetic form factors.

No ground state experimental data are available for the elastic $C2$ longitudinal form factor in $^{27}$Al. The $C2$ form factor is available for other states. We choose the first excited state $1/2^-$ at 0.844 MeV. The $C2$ calculations are presented in Fig. 5(a) with the MS contribution (dashed curve) and with the inclusion of CP (solid curve). The experimental data are very well explained with CP for all momentum transfer except at the region of the diffraction minimum. The effective charges deduced from the CP calculation at the photon point, are $e_p = 1.23e$ and $e_n = 0.49e$. The form factors calculated with MS wave functions but with the above effective charges are displayed in Fig. 5(b) in comparison with that including CP and the experimental data. The experimental data are very well explained by both models for the CP. The $B(E2)$ value is $14.75e^2\,\mathrm{fm}^4$ in comparison with the experimental value $12.79 \pm 0.5e^2\,\mathrm{fm}^4$ [41]. The $B(E2)$ value enhances by about a factor of 4 by CP. Enhancement of the $C2$ form factor is noticed with the inclusion of CP effects by about a factor of 4

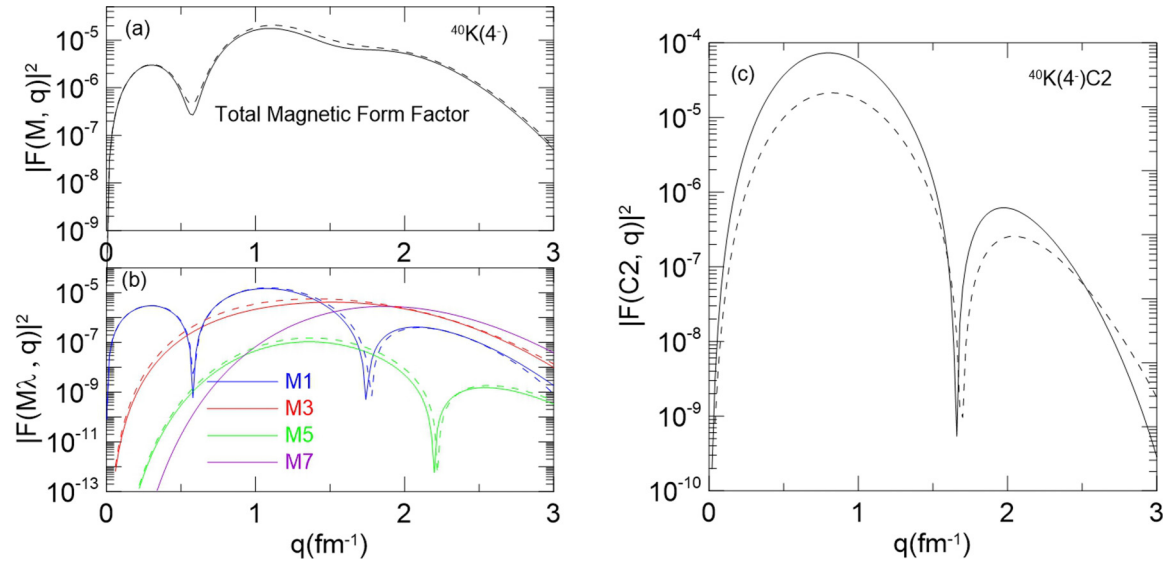


FIG. 12. Elastic magnetic form factors (a) with the contribution of the different multipolarities (b) and $C2$ longitudinal form factor (c) for $4^-$ ground state of $^{40}$K. Dashed curves represent the MS form factors and the solid curves represent the MS + CP form factors.

at the position of the maximum form factor (at $q = 1\,\mathrm{fm}^{-1}$). The core-polarization contribution, shown in Fig. 6 as cross symbols, is very close to the MS contribution.

## IV. CONCLUSIONS

We have investigated the microscopic structure of the neutron-rich *sd-pf* cross-shell nuclei. The nature and origin of the quadrupole collectivity that develops for $N > 20$ are discussed by comparing the measured magnetic and $Q$ moments with shell model calculations. CP with particle-hole excitation has no effect on the magnetic moment (at the photon point), but small suppression is noticed for $q$-dependent form factors since most of the nucleon spins and orbital momenta pair off to yield zero contribution, for which the nuclear magnetism thus is determined by a few valence nucleons, with an almost negligible effect of CP.

There is reasonable agreement between the measured and calculated magnetic moments for most of the isotopes considered in this work using free nucleon $g$ factors. Few of them are with opposite sign. Effective $g$ factors resolve this discrepancy for these isotopes, except for $^{40}$Ar. CP enhances the $Q$ moment and gives a reasonable description of the experimental values. The effective charges deduced from CP calculations are less than the standard ones. In general, calculations show quenching of effective charges in neutron-rich nuclei, incorporating the decoupling feature of loosely bound particles. For the $Q$ moment of the $^{43}$Ar isotope, the BM model gives better agreement with the measured value than that of the CP value, where the enhanced collectivity at $N = 25$ may reduce the $N = 28$ shell gap for this large neutron excess isotope, which gives a high quadrupole moment, which is well described by the collective model with the BM effective charges. Most of the measured magnetic moments for the ground state of potassium (K) isotopes are well described by effective nucleon $g$ factors. Effective nucleon $g$ factors predict the correct sign for all K isotopes considered in this work.


[1] H. Sagawa and K. Asahi, Phys. Rev. C **63**, 064310 (2001).
[2] H. Ogawa, K. Asahi, K. Sakai, T. Suzuki, H. Izumi, H. Miyoshi, M. Nagakura, K. Yogo, A. Goto, T. Suga, T. Honda, H. Ueno, Y. X. Watanabe, K. Yoneda, A. Yoshimi, N. Fukuda, Y. Kobayashi, A. Yoshida, T. Kubo, M. Ishihara, N. Imai, N. Aoi, W.-D. Schmidt-Ott, G. Neyens, and S. Teughels, Phys. Rev. C **67**, 064308 (2003).
[3] A. Bohr and B. R. Mottelson, *Nuclear Structure* (Benjamin, New York, 1975), Vol. 2, p. 515.
[4] H. Sagawa and B. A. Brown, Nucl. Phys. A **430**, 84 (1984).
[5] C. Forssén, J. P. Vary, E. Caurier, and P. Navrátil, Phys. Rev. C **77**, 024301 (2008).
[6] A. Umeya, G. Kaneko, and K. Muto, Nucl. Phys. A **829**, 13 (2009)
[7] G. Co', V. De Donno, P. Finelli, M. Grasso, M. Anguiano, A. M. Lallena, C. Giusti, A. Meucci, and F. D. Pacati, Phys. Rev. C **85**, 024322 (2012).
[8] A. D. Davies, A. E. Stuchbery, P. F. Mantica, P. M. Davidson, A. N. Wilson, A. Becerril, B. A. Brown, C. M. Campbell, J. M. Cook, D. C. Dinca, A. Gade, S. N. Liddick, T. J. Mertzimekis, W. F. Mueller, J. R. Terry, B. E. Tomlin, K. Yoneda, and H. Zwahlen, Phys. Rev. Lett. **96**, 112503 (2006).
[9] Z. Wang, Z. Ren, T. Dong, and X. Guo, Phys. Rev. C **92**, 014309 (2015).
[10] R. F. Garcia Ruiz, M. L. Bissell, K. Blaum, N. Frömmgen, M. Hammen, J. D. Holt, M. Kowalska, K. Kreim, J. Menéndez, R. Neugart, G. Neyens, W. Nörtershäuser, F. Nowacki, J. Papuga, A. Poves, A. Schwenk, J. Simonis, and D. T. Yordanov, Phys. Rev. C **91**, 041304(R) (2015).
[11] G. Co', V. De Donno, M. Anguiano, R. N. Bernard, and A. M. Lallena, Phys. Rev. C **92**, 024314 (2015).
[12] A. Saxena and P. C. Srivastava, Phys. Rev. C **96**, 024316 (2017).
[13] B. Alex Brown and W. A. Richter, Phys. Rev. C **74**, 034315 (2006).
[14] M. Bouhelal, M. Labidi, F. Haas, and E. Caurier, Phys. Rev. C **96**, 044304 (2017).
[15] E. Garrido and E. Moya de Guerra, Nucl. Phys. A **650**, 387 (1999).
[16] E. Garrido and E. Moya de Guerra, Phys. Lett. B **488**, 68 (2000).
[17] A. N. Antonov, M. K. Gaidarov, D. N. Kadrev, P. E. Hodgson, and E. Moya de Guerra, Int. J. Mod. Phys. E **13**, 759 (2004).
[18] A. N. Antonov, D. N. Kadrev, M. K. Gaidarov, E. Moya de Guerra, P. Sarriguren, J. M. Udias, V. K. Lukyanov, E. V. Zemlyanaya, and G. Z. Krumova, Phys. Rev. C **72**, 044307 (2005).
[19] C. A. Bertulani, J. Phys. G: Nucl. Part. Phys. **34**, 315 (2007).
[20] A. N. Antonov, M. K. Gaidarov, M. V. Ivaniv, D. N. Kaderev, M. Aïche, G. Barreau, S. Czajkowsk, B. Jurado, G. Belier, and A. Chatillon, Nucl. Instrum. Methods Phys. Res., Sect. A **637**, 60 (2011).
[21] P. J. Brussaard and P. W. M. Glaudemans, *Shell Model ApplicationsIn Nuclear Spectroscopy* (North Holland, Amsterdam, 1977).
[22] G. Berstch, J. Borysowicz, H. McManus, and W. G. Love, Nucl. Phys. A **284**, 399 (1977).
[23] B. A. Brown, B. H. Wildenthal, C. F. Williamson, F. N. Rad, S. Kowalski, H. Crannell, and J. T. O'Brien, Phys. Rev. C **32**, 1127 (1985).
[24] I. Tanihata, H. Savajols, and R. Kanungo, Prog. Part. Nucl. Phys. **68**, 215 (2013).
[25] B. A. Brown and W. D. M. Rae, Nucl. Data Sheets **120**, 115 (2014).
[26] NuShellX, W.D.M. Rae, http://www.garsington.eclipse.co.uk.
[27] F. Nowacki and A. Poves, Phys. Rev. C **79**, 014310 (2009).
[28] I. Angeli and K. P. Marinova, At. Data Nucl. Data Tables **99**, 69 (2013).
[29] B. A. Brown, R. Radhi, and B. H. Wildenthal, Phys. Rep. **101**, 313 (1983).
[30] N. J. Stone, IAEA Vienna Report No. INDC(NDS)-0658 (2014).
[31] E. A. Stefanova, N. Benczer-Koller, G. J. Kumbartzki, Y. Y. Sharon, L. Zamick, S. J. Q. Robinson, L. Bernstein, J. R. Cooper, D. Judson, M. J. Taylor, M. A. McMahan, and L. Phair, Phys. Rev. C **72**, 014309 (2005).
[32] J. Papuga, M. L. Bissell, K. Kreim, K. Blaum, B. A. Brown, M. De Rydt, R. F. Garcia Ruiz, H. Heylen, M. Kowalska, R. Neugart,

G. Neyens, W. Nörtershäuser, T. Otsuka, M. M. Rajabali, R. Sa´nchez, Y. Utsuno, and D. T. Yordanov, Phys. Rev. Lett. **110**, 172503 (2013).
[33] W. A. Richter, S. Mkhize, and B. Alex Brown, Phys. Rev. C **78**, 064302 (2008).
[34] A. E. Stuchbery, A. D. Davies, P. F. Mantica, P. M. Davidson, A. N. Wilson, A. Becerril, B. A. Brown, C. M. Campbell, J. M. Cook, D. C. Dinca, A. Gade, S. N. Liddick, T. J. Mertzimekis, W. F. Mueller, J. R. Terry, B. E. Tomlin, K. Yoneda, and H. Zwahlen, Phys. Rev. C **74**, 054307 (2006).
[35] B. Pritychenko, M. Birch, and M. Horoi, At. Data Nucl. Data Tables **107**, 1 (2016).
[36] C. M. Campbell, N. Aoi, D. Bazin, M. D. Bowen, B. A. Brown, J. M. Cook, D.-C. Dinca, A. Gade, T. Glasmacher, M. Horoi, S. Kanno, T. Motobayashi, L. A. Riley, H. Sagawa, H. Sakurai, K. Starosta, H. Suzuki, S. Takeuchi, J. R. Terry, K. Yoneda, and H. Zwahlen, Phys. Lett. B **652**, 169 (2007).
[37] K. Kaneko, Y. Sun, T. Mizusaki, and M. Hasegawa, Phys. Rev. C **83**, 014320 (2011).
[38] P. J. Ryan, R. S. Hicks, A. Hotta, J. Dubach, G. A. Peterson, and D. V. Webb, Phys. Rev. C **27**, 2515 (1983).
[39] T. W. Donnelly and I. Sick, Rev. Mod. Phys. **56**, 461 (1984).
[40] T. Suzuki, Phys. Lett. B **120**, 27 (1983).
[41] P. M. Endt and C. van der Leun, Nucl. Phys. A **310**, 1 (1978).